metals

MDPI

Article

Processing, Microstructure, and Properties of Bimetallic Steel-Ni Alloy Powder HIP

Shenyan Huang [1,*], Chen Shen [1] and Victor Samarov [2]

[1] GE Research, Niskayuna, NY 12309, USA
[2] Synertech PM, Garden Grove, CA 92841, USA
* Correspondence: huangs@ge.com

Abstract: This work explores technical feasibility in hot isostatic pressing (HIP) manufacturing of an integral bimetallic component using steel and Ni alloy powder for supercritical carbon dioxide (sCO_2) turbomachinery. Lab-scale bimetallic HIP specimens using HAYNES® 282® and SS316L or SS415 powder are investigated in powder configuration, heat treatment, microstructure, and tensile properties up to 400 °C. Interdiffusion profiles at dissimilar alloy interfaces caused by HIP cycle is predicted by DICTRA simulations and validated by electron probe microanalysis (EPMA). The interdiffusion distance of most elements is around 100 µm, while C and N have a higher interdiffusion distance. Dense distribution of Ti-rich carbonitrides and alumina particles are found to decorate prior particle boundaries near joining interface on the 282 side, affecting tensile strength across interface as well as tensile failure location. A higher amount of excessive carbonitride formation near interface is observed in SS316L/282 than in SS415/282, which is consistent with the predicted greater degree of interdiffusion effect in SS316L/282. Typical HAYNES® 282® heat treatment condition is applicable to 282/SS316L and 282/SS415 combinations, resulting in a higher strength than cast CF8M and CA6NM. A pilot-scale bimetallic SS415/282 pipe is then demonstrated to show the promise of scaleup.

Keywords: hot isostatic pressing; powder metallurgy; steel; superalloy; dissimilar metal joining

Citation: Huang, S.; Shen, C.; Samarov, V. Processing, Microstructure, and Properties of Bimetallic Steel-Ni Alloy Powder HIP. *Metals* **2024**, *14*, 118. https://doi.org/10.3390/met14010118

Academic Editors: Leszek Adam Dobrzański and Joan-Josep Suñol

Received: 26 December 2023
Revised: 14 January 2024
Accepted: 15 January 2024
Published: 19 January 2024

1. Introduction

A high-temperature supercritical carbon dioxide (sCO_2) power cycle is being developed for concentrating solar-thermal power (CSP) application, providing more compact size and higher efficiency than a conventional steam power cycle [1]. A sCO_2 turbine that operates above 700 °C will require the use of γ' strengthened Ni-based superalloys for turbomachinery components at hot sections, leading to higher component cost than the lower temperature cycles that use structural steels. High cost is associated with manufacturing challenges and supply chain limitations of forging, casting, and machining large complex components in newer superalloys that are not broadly practiced such as HAYNES® 282® (Haynes International. Inc., Kokomo, IN, USA) and Inconel 740 H. Recently, alternative manufacturing modality of powder metallurgy (PM) near-net-shape (NNS) HIP has been demonstrated in a 10 MW sCO_2 turbine casing prototype, proving a significant reduction in component cost and levelized cost of electricity (LCOE) for CSP [2]. The present work further explores the technical feasibility in HIP manufacturing of an integral bimetallic component using steel and Ni alloy powder, which potentially further reduces powder cost by replacing Ni alloy partially with steel at lower temperature locations.

HIP diffusion bonding has been studied to join two similar or dissimilar metals in solid forms. Compared to conventional diffusion bonding that involves a uniaxial low pressure and limited plasticity, HIP diffusion bonding uses isostatic pressure in higher magnitude to increase diffusion rate and plasticity to achieve a sound metallurgical bonding that is free of voids [3]. The solid-state nature of the HIP process allows improved bonding strength compared to fusion welds (due to lack of heat affected zone and fusion zone) and

joining of difficult-to-weld alloys (i.e., oxide dispersion strengthened alloys) [4–6]. In other papers, this process is also called HIP cladding where powder-to-solid or solid-to-solid HIP diffusion bonding forms a conformal layer that is thicker than what conventional coating processes could achieve [7–9]. The effect of pressure applied by HIP is reported to change precipitation kinetics, thus affecting the diffusion rate and grain structure at the interface of Fe-Al and CrMo steel [10]. HIP diffusion bonding also has fewer limitations in component geometry and size than conventional diffusion bonding. A variety of components in material combinations of Ni, Co, Ti, or steel alloys have been produced including valve body, well head, flywheel, extrusion dies, grinding roll for corrosion and wear-resistant applications, and turbine blisks [3,7–9,11–13]. Feasibility of HIP bonding Ni superalloy and Mo-Re refractory alloy, dissimilar Vanadium alloys, Cu alloy and Ni alloy, stainless steel and Ni alloy, and stainless steel and Ti alloy have been studied at lab-scale [14–17]. To the best of our knowledge, powder-to-powder HIP diffusion bonding has rarely been studied [18–20]. The powder-to-powder route was considered to be optimal due to the possibility of forming mechanical locks at the interface and local deformation of the particles at the interface for a better diffusion. Dissimilar powder bonding using spark plasma sintering (SPS) was studied for Inconel 718 and RR 1000 that resulted in no defects, intermetallic phases, and prior particle boundaries (PPB) at the bonding interface [21]. Despite the advantage of a shorter heating cycle in SPS to control kinetics of phase formation and grain coarsening, SPS does not have the scalability for large components with complex shapes, as the powder HIP approach has proven.

A HIP bonding strength with minimal penalties in mechanical properties highly relies on the alloy compositions, HIP cycle, post heat treatment, and interface preparation for cleanliness before HIP, which govern the resulting composition and phases, grain structure, and residual stress at bonding interface. Solid-to-solid HIP diffusion bonding requires low surface roughness, high cleanliness, and oxide-free bonding interface ensured by a physical or chemical interface preparation method prior to HIP [3,22]. The HIP temperature and post-HIP heat treatment shall be carefully balanced to reduce interface voids and prevent severe grain coarsening. Interlayer in solid state or melted state during the HIP cycle could be used at the joint interface to change the microstructure and composition, however, interlayer does not always benefit mechanical properties [23,24]. Similarly, powder HIP diffusion bonding requires a capsule containment of powder and sufficient outgassing followed by a leak check to ensure no leakage and contamination during HIP. Powder HIP has the advantage of finer grain size and thus potentially a wider window of HIP and heat treatment conditions. For dissimilar metal HIP, an interdiffusion zone up to hundreds of μm forms after HIP cycle, providing a transition in composition and coefficient of thermal expansion (CTE). This interdiffusion zone often prevents a sharp interface and reduces CTE mismatch-induced localized stress [11]. However, the formation of detrimental phases, dissolution or formation of carbides, and sharp concentration gradient within this interdiffusion zone may embrittle this region and significantly impact mechanical properties of the HIP bonding. Bonding interface between steel and Ni alloy could have complicated phases depending on the alloy combinations. For example, the interdiffusion zone between Ni-based Astroloy powder alloy and low carbon steel capsule was reported to contain five distinct sub layers of martensite, austenite, intense carbide precipitation zone, Fe-Ni rich superalloy, and Ni-Fe rich superalloy, whereas γ' precipitate size and fraction also varied within these layers [25]. Chemical potential and activity difference affects carbon diffusion at the interface, which in turn affects carbide type/size/fraction, phase of steel, and martensite phase transformation temperature. For example, dissimilar HIP bonding between tool steel (0.82% C) and martensitic steels (0.16–0.98% C) have distinct carbon profiles and diffusion distance at interface, where elevated carbon due to uphill diffusion occurs in one case [26]. PPB oxides and carbides formation due to carbon diffusion cause unsatisfactory properties in powder-to-solid HIP joints of SA508 and SS316L [27]. Additionally, phase transformation occurs during HIP or post heat treatments (such as austenite-martensite transformation in steel) which creates localized stress at the interface and increases the risk of cracking [8,26,28].

Thus, optimizing HIP diffusion bonding of dissimilar alloys requires a deep understanding of processing-structure-property relationships.

In the present work, bimetallic powder HIP between HAYNES® 282® and SS316L or SS415 is investigated computationally and experimentally. Using lab-scale HIP material, several configurations with different powder heat treatment conditions are studied. The interdiffusion profile at dissimilar alloy interface as a result of HIP cycle is understood by diffusion simulation using DICTRA and microstructure characterization. The strength of HIP bonding is measured by cross-interface tensile tests and compared against cast alloys. The role of carbonitride formed by carbon diffusion near interface is implied. A pilot-scale bimetallic pipe is then demonstrated to show some level of scalability.

2. Materials and Methods

Compositions of the studied alloy powders are listed in Table 1. Plasma atomized 282 alloy powder with size range of 20–180 μm and relative tap density of 67% was acquired from AP&C (Montreal, QC, Canada), a GE Additive company (Montreal, QC, Canada). Despite the higher cost than GA powder, PA powder has the advantages of improved cleanliness (i.e., N, O), highly spherical morphology, low trapped gas/porosity, and high yield in the powder size range that make it appropriate for PM HIP. Nitrogen gas atomized SS316L powder with size range of 44–106 μm and relative tap density of 60% was acquired from Carpenter Technology (Philadelphia, PA, USA). Two custom lots of argon gas atomized SS415 with a size range of 20–180 μm were acquired from Praxair Surface Technologies (Indianapolis, IN, USA). Relative tap density of the two lots were 64% and 60%, respectively. The first lot had lower carbon than expected, while the second lot had higher carbon, consistent with typical SS415.

Table 1. Actual powder alloy compositions (in wt.%).

Alloy	Ni	Co	Fe	Cr	Al	Ti	Mo	C	Mn	Si	N	O
SS316L powder	12.6	-	Bal.	17.82	-	-	2.32	0.021	0.96	0.71	0.09	0.015
SS415#1 powder	4.9	-	Bal.	12.9	-	-	0.74	0.002	0.61	0.08	0.003	0.063
SS415#2 powder	4.6	-	Bal.	12.2	-	-	0.76	0.028	0.75	0.03	0.01	0.031
282 powder	Bal.	9.95	0.95	19.5	1.44	2.09	8.26	0.067	0.15	0.084	0.006	0.007

To understand the interdiffusion and phase evolution at the interface between steel and 282 alloy during the HIP cycle, diffusion (DICTRA) simulations were employed to predict composition profiles across the interface and the resulting phases. In all simulations, the steel (either SS316L or SS415) was placed on the left and the 282 alloy was placed on the right, with a sharp interface in the middle initially. The length of either side was four mm, sufficient to cover the full diffusion distance of the (faster diffusion) interstitial elements, C and N, over the full HIP time-temperature cycle. A non-uniform grid was used to allow a fine resolution (grid spacing) within the interface region, at about one (center) to seven microns.

Austenite-martensite phase transformation temperatures upon heating and cooling in HIPed SS415 was measured by differential scanning calorimetry (DSC) using Netzsch STA 449C (Netzsch Instruments North America, Burlington, MA, USA). An yttria-coated, alumina-lined Pt-Rh crucible was used to hold a small specimen during DSC measurement. A heating and cooling rate of 10 °C/min and temperature up to 1500 °C were applied. Additionally, CTE and density of HIPed SS415 were measured by Netzsch DIL 402SU dilatometry up to 1200 °C, using a pin specimen with 25 mm length and 6 mm diameter. These results provide practical considerations on the post heat treatment condition and dimensional estimate after HIP.

Several conditions of steel/282 bimetallic powder HIP were created to study the interface microstructure and strength, as summarized in Table 2. Small HIP cans in SS304 with 19 mm diameter and 50 mm height were used for a microstructure study. Taller HIP cans in SS304 with 30 mm diameter and 180 mm height were used for mechanical property evaluation. One alloy powder was first filled in the bottom half of the can. Then the can containing half-filled powder was heat treated in a vacuum furnace at either 1000 °C or 1100 °C for 30 min, to allow slight sintering of powder at surface and forming an immobile powder surface. Then another alloy powder was filled in the top half, followed by standard powder vibrational packing. The powder vacuum heat treatment was shown to successfully maintain a sharp dissimilar powder interface during powder packing. The can was outgassed at both room temperature and an elevated temperature to achieve acceptable leak up rate before being pinched off. A helium leak check was conducted to ensure the integrity of the can prior to sealing. The same HIP cycle of 1204 °C/15 ksi/4 h was applied on all the studied conditions to fully densify powder, using either 6–45 H or 14–30 H HIP unit at American Isostatic Presses. During HIP cycle, temperature and pressure were ramped simultaneously to the set points with a 10 °C/min ramp rate. After the temperature and pressure soak, pressure was released, and a natural furnace cooling was performed. Examples of the small and taller cans after HIP are shown in Figure 1. The typical HAYNES® 282® heat treatment procedure was applied after HIP cycle, including solution treatment (1149 °C/1 h/WQ) followed the by two-step aging treatments (1010 °C/2 h/AC + 788 °C/8 h/AC).

(**a**) (**b**)

Figure 1. Examples of a small can loaded with SS316L and 282 powder (**a**) and a taller can loaded with SS316L and 282 powder (**b**) after HIP cycle.

Representative microstructures in as-HIP and heat-treated states were obtained by high-resolution backscattered electron imaging using a Hitachi SU-70 FEG-SEM (Hitachi High-Tech America, Inc., Schaumburg, IL, USA) with a Bruker XFlash 6-60 SDD EDS detector (Bruker, Billerica, MA, USA). Composition profiles across interfaces were measured by Electron Probe Micro-analysis (EPMA) using the JEOL 8530F microprobe (JOEL USA Inc., Ashland, OR, USA). The analyses were made at 15 kV, 50 nA beam current, with a three micrometer beam diameter and three micrometer step increments.

Screw-threaded dog bone tensile specimens were machined from the base metal of SS316L, SS415, 282, and across steel/282 interface. The specimens had 3.5 mm gauge diameter, 19 mm gauge length, 6.35 mm grip diameter, and 50 mm total length. No issue was experienced in machining the steel/282 bimetallic specimens using the same machining procedure. Tensile tests were performed at room temperature, 200 °C, and 400 °C with 1–2 repetitions at the same test condition. A constant displacement rate of 0.5 mm/min was imposed for each test, and an extensometer was applied at the specimen gauge to measure strain evolution.

Table 2. The studied conditions of steel/282 bimetallic powder HIP.

Bimetallic Configuration	Powder Filled in Bottom Half Can	Powder Vacuum Heat Treatment	Powder Filled in Top Half Can	HIP Cycle	Solution and Aging Treatments	Tempering Treatment
282/SS316L	SS316L	1000 °C/30 min	282	1204 °C 15 ksi 4 h	1149 °C/1 h/WQ 1010 °C/2 h/AC 788 °C/8 h/AC	N/A
SS316L/282	282	1100 °C/30 min	SS316L			N/A
282/SS415#1	SS415#1	1000 °C/30 min	282			600 °C/1 h
SS415#1/282	282	1100 °C/30 min	SS415#1			600 °C/1 h
282/SS415#2	SS415#2	1000 °C/30 min	282			N/A

N/A is not applicable.

3. Results

3.1. Interdiffusion Simulation and Phase Prediction for HIP Cycle

The simulated composition profiles of SS316L/282 and SS415/282 are shown in Figures 2 and 3, respectively, for a simplified full HIP cycle of 4 h at 1204 °C, i.e., without the heating and cooling portions. The actual powder compositions in Table 1 (SS316L powder, SS415#1 powder, and 282 powder) were used. The alternate composition, SS415#2 powder, was also simulated but the results are not shown here due to their insignificant differences. After diffusion, steep slopes of some elements (Ti, Cr, C, N, Si) were developed as a result of phase formation at the joining interface. In particular, C and N peaks are associated with MC (as Ti (C,N)) phase formation. It is also noted that non-linear Si segregation profiles were predicted in SS415/282, even though the difference in the bulk compositions was small.

Equilibrium phases were simulated with the final compositions from the interdiffusion simulations for both SS316L/282 and SS415/282. To compare them against the microstructures from actual specimens, the phase calculations were made at the final aging temperature of 788 °C. It is clearly shown in Figure 4 that there was a greater influence of interdiffusion to SS316L/282, as shown by the γ' phase profiles at the 282 side from the interface. It is evident that a higher amount of carbide (MC) phase was predicted in the SS316L case than in the SS415 case, however, both show the excess carbide formation on the 282 side of the initial interface.

For a more quantitative comparison among elements and between the two materials (SS316L and SS415), interdiffusion distance ("IDZ width") was extracted from the simulated composition profiles. In Figure 5a, all elements show a characteristic trend of square root of time for diffusion-limited processes. As expected, the interstitial elements C and N have higher diffusion rates than the substitutional (metallic) elements. C and N diffusion is similar between SS316L and SS415. Among the metallic elements, Si is among the fastest elements. Ni (not shown in the plot) has an almost identical diffusion rate as Fe. Most of these elements have nearly the same diffusion rate between SS415 and SS316L, except for Ti and Cr, which are slower in SS415. Overall, the response of interdiffusion distance to HIP temperature is similar between SS316L/282 and SS415/282. The interdiffusion distance varies among elements, with most elements being at about 100 μm (between Ti and Fe), Si and Cr about twice wider, and C, N far exceeding all the formers.

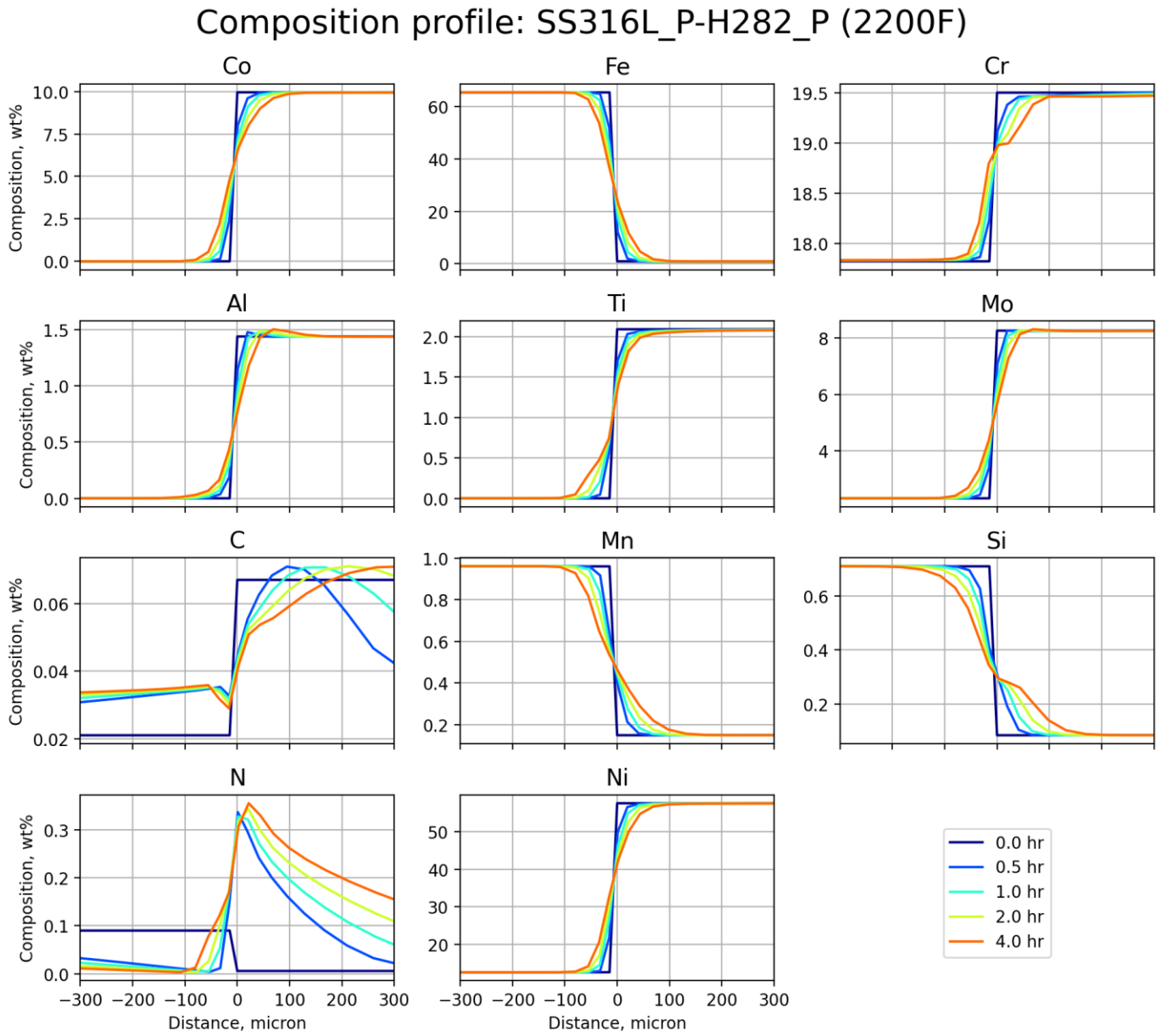

Figure 2. Simulated interdiffusion profiles between SS316L (**left**) and 282 (**right**) at 1204 °C (HIP temperature). Joining interface is in the middle.

3.2. SS415 Phase Transformation and Thermal Properties

Austenite/martensite phase transformation temperatures in SS415#1 were obtained by DSC analysis, as shown in Figure 6. Upon heating, the broad endotherm from 400 °C to 770 °C is likely due to overlap of the Curie magnetic transition (peak at 677 °C) and martensite to austenite transformation (peak at 707 °C). A smaller exotherm from 400 °C to 550 °C overlaps with the larger endotherm, probably due to an additional phase transition. Upon cooling, the exotherm with an onset of 398 °C and peak at 374 °C is likely due to austenite to martensite transition. Dilatometry analyses are presented in Figure 7. The ~0.2% linear shrinkage (~0.6% volumetric shrinkage) and density increase from about 657 °C to 718 °C is caused by martensite to austenite transformation, consistent with DSC observation. As a result, mean CTE and differential CTE both show a sharp drop around transformation temperature. Phase transformation temperature for SS415#2 was not measured, but martensite start temperature with the presence of higher carbon is anticipated to be slightly higher than SS415#1 (within 10 °C). The dimensional change due to phase transformation was considered in the HIP model to accurately predict the HIP

shrinkage and reverse design the HIP tooling for a bimetallic pipe component (as described in Section 3.5).

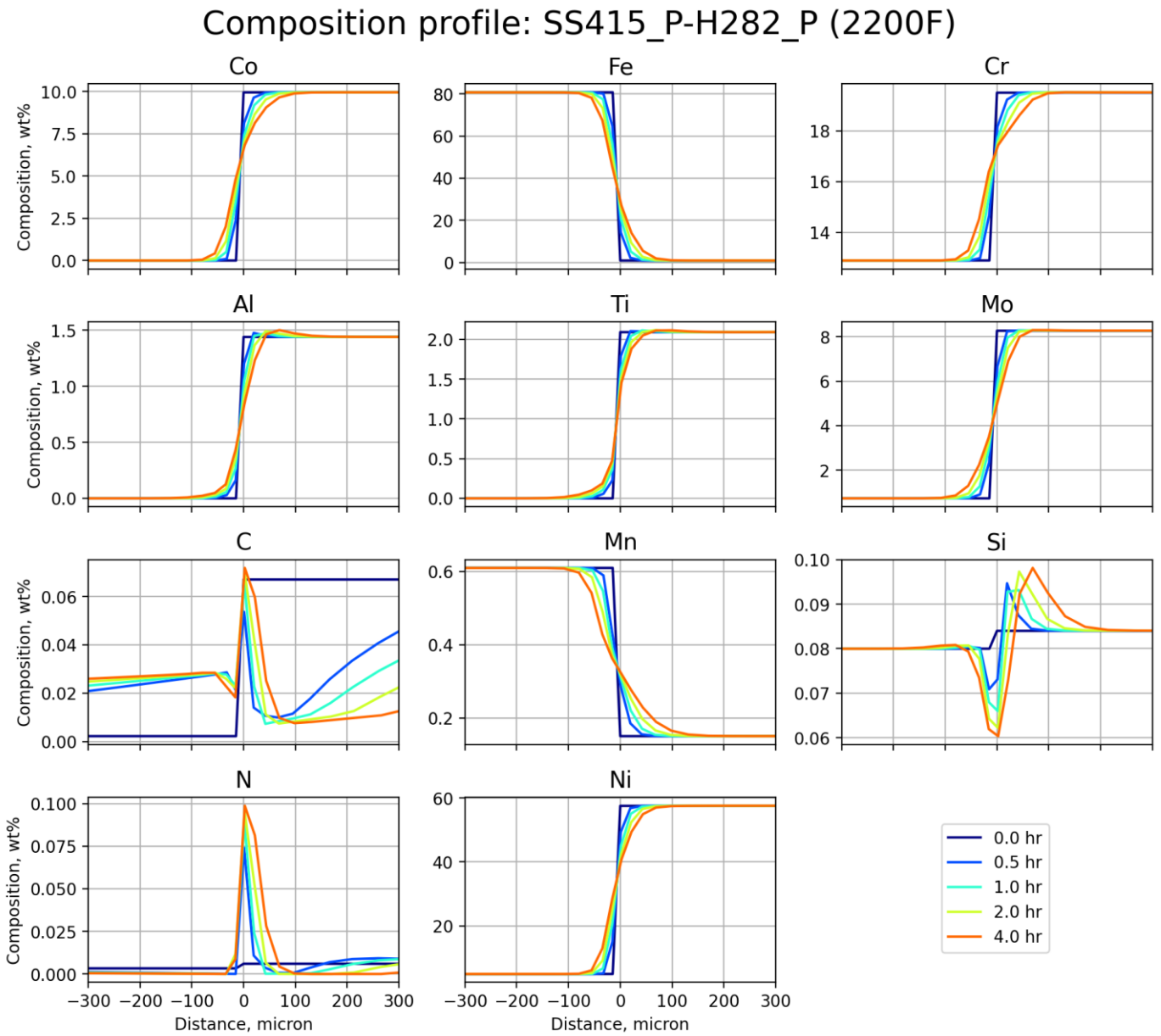

Figure 3. Simulated interdiffusion profiles between SS415 (#1 powder) and 282 (**right**) at 1204 °C (HIP temperature). Joining interface is in the middle.

3.3. Heat Treatment after HIP

The heat treatment of bimetallic powder HIP needs to satisfy the requirements of (1) being suitable for both 282 and SS316L or SS415 simultaneously, and (2) being suitable for the joining interface (transition region). The typical heat treatment conditions for the three alloys are listed in Table 3.

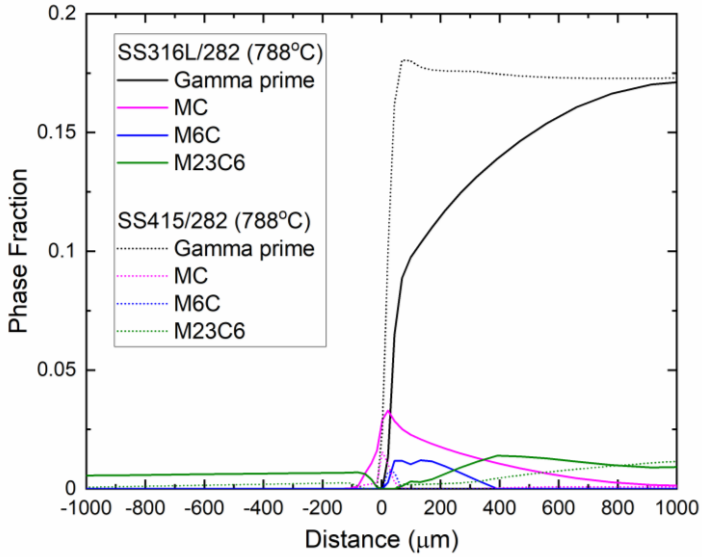

Figure 4. Simulated equilibrium phases at aging temperature 788 °C across interdiffusion zone of SS316L/282 and SS415/282.

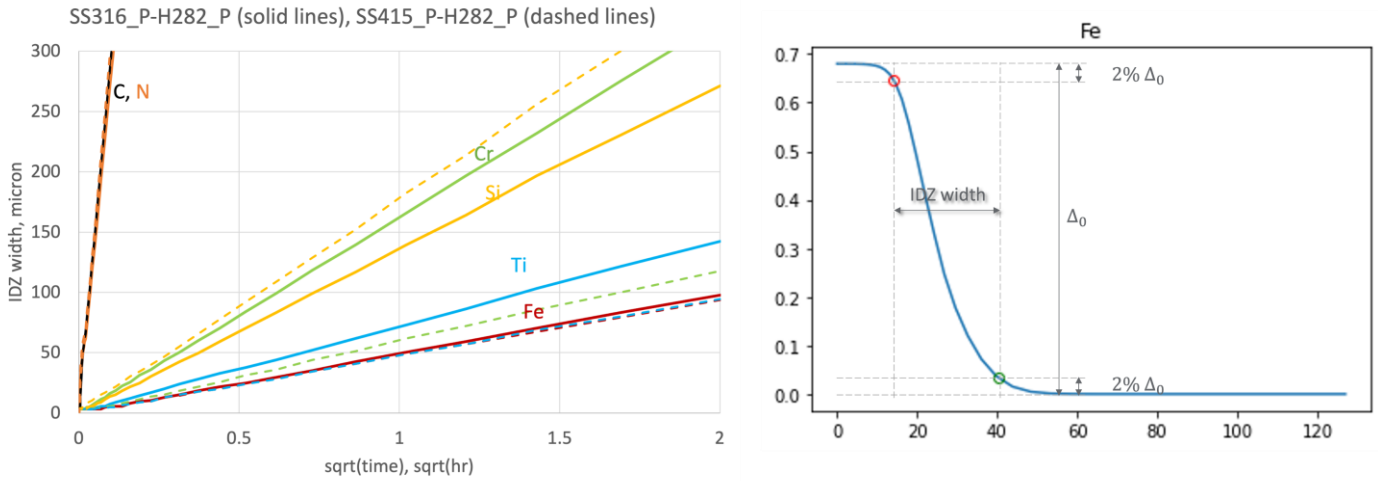

(**a**) (**b**)

Figure 5. (**a**) Comparison of the simulated interdiffusion zone (IDZ) width of selected elements for SS316L/282 and SS415/282 at 1204 °C (HIP temperature), (**b**) definition of IDZ width adopted in the plot.

Among these conditions, the solution/annealing of HAYNES® 282® (1121–1149 °C) and aging step 1 (1010 °C) are comparable to the annealing step of SS316L and the hardening step (i.e., austenitization followed by a quench to martensite) of SS415. Calculated phase diagrams (Figure 8) also suggest that 1010–1149 °C is well within the austenite temperature range of SS316L and SS415. Therefore, it is possible to replace the annealing step of SS316L and the hardening step of SS415 with the solution/annealing (and aging step 1) of HAYNES® 282®.

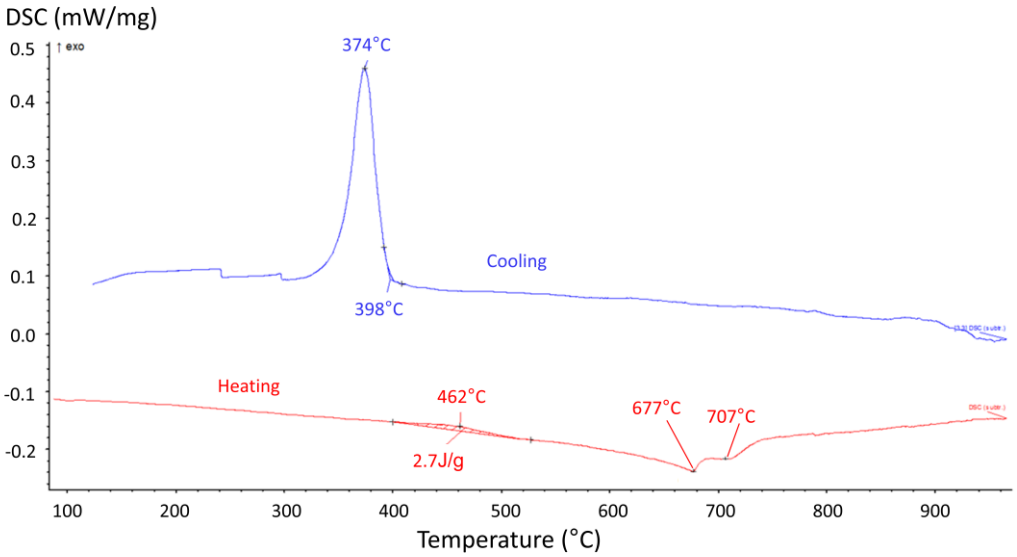

Figure 6. DSC heat flow vs. temperature for PM HIP SS415#1.

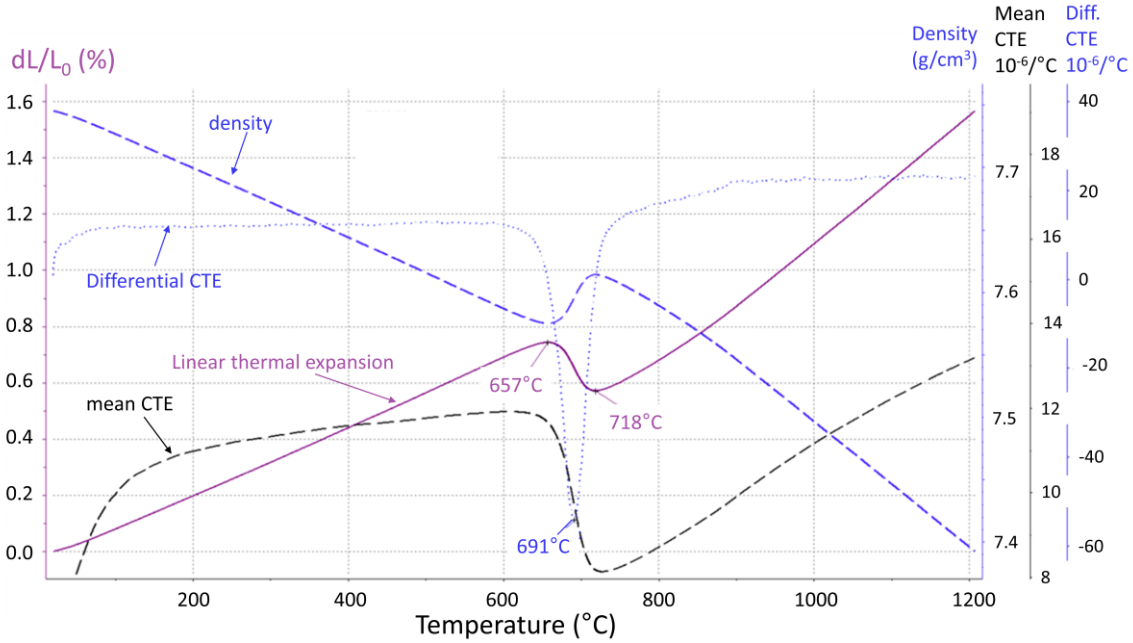

Figure 7. Thermal expansion, mean CTE, differential CTE, and density vs. temperature for PM HIP SS415#1 measured by dilatometry.

The main concern, however, is in regard to the 788 °C or 800 °C aging step of HAYNES® 282®. Firstly, SS316L is prone to formation of (Cr-rich) sigma and χ phases between 650–870 °C during an extended exposure, which can lead to reduction in mechanical properties and corrosion resistance (sensitization). The 788 °C/8 h or 800 °C/4 h aging step of 282 is within this window, as compared to a published TTT diagram for SS316L [29]. Several short-term heat treatment experiments were performed. Microstructural characterization verified that both aging conditions are safe to SS316L without causing brittle sigma and χ phases at grain boundaries. Therefore, solution and two-step aging of HAYNES® 282® was recommended for bimetallic HIP of SS316L/282 combinations.

Table 3. The typical heat treatment conditions for HAYNES® 282®, SS316L, and SS415 alloys.

HAYNES® 282®	SS316L	SS415
Solution/annealing: 1121–1149 °C, air cool (AC), Two-step Aging: 1010 °C for 2 h, AC; 788 °C for 8 h, AC. Or single-step Aging: 800 °C for 4 h, AC.	Annealing: 1040–1105 °C, AC.	Hardening: (except for +A) 950–1050 °C, AC or oil cool Tempering: 600–650 °C, AC or furnace cool ("soft annealed" +A); 650–700 °C, 600–620 °C, AC or furnace cool ("quench-tempered" QT650) 550–600 °C, AC or furnace cool (QT780) 520–580 °C, AC or furnace cool (QT900)

Regarding SS415, the 788 °C/8 h or 800 °C/4 h aging step is above the usual tempering temperature window of SS415 mentioned prior. According to calculations (Figure 8), the temperatures are already into the lower end of the austenitic region of SS415. Combined with DSC analysis on PM SS415 (Figure 6), the martensite to austenite transformation occurs at 707–724 °C. Thus, a viable way for SS415 appears to combine HAYNES® 282® heat treatment and a subsequent tempering step at a lower temperature 600 °C. A tempering time of 1, 2, and 3 h was tested. It was expected that this tempering step would not affect the microstructure of 282 since 600 °C is lower than the two-step aging temperature of 282 (788 °C). Microhardness was performed on small coupons in various conditions, including as-HIP state, solution and two-step aging with/without tempering, solution and 1-step aging with/without tempering. As-HIP, solutioned, and aged conditions all show high hardness values above 280 HV. With tempering, hardness drops to 230–235 HV. The tempered samples with different soak time all have similar hardness values. The two-step aging and one-step aging conditions did not show a big difference. Therefore, 600 °C/1 h tempering was downselected and applied to the 282/SS415#1 subscale HIP samples.

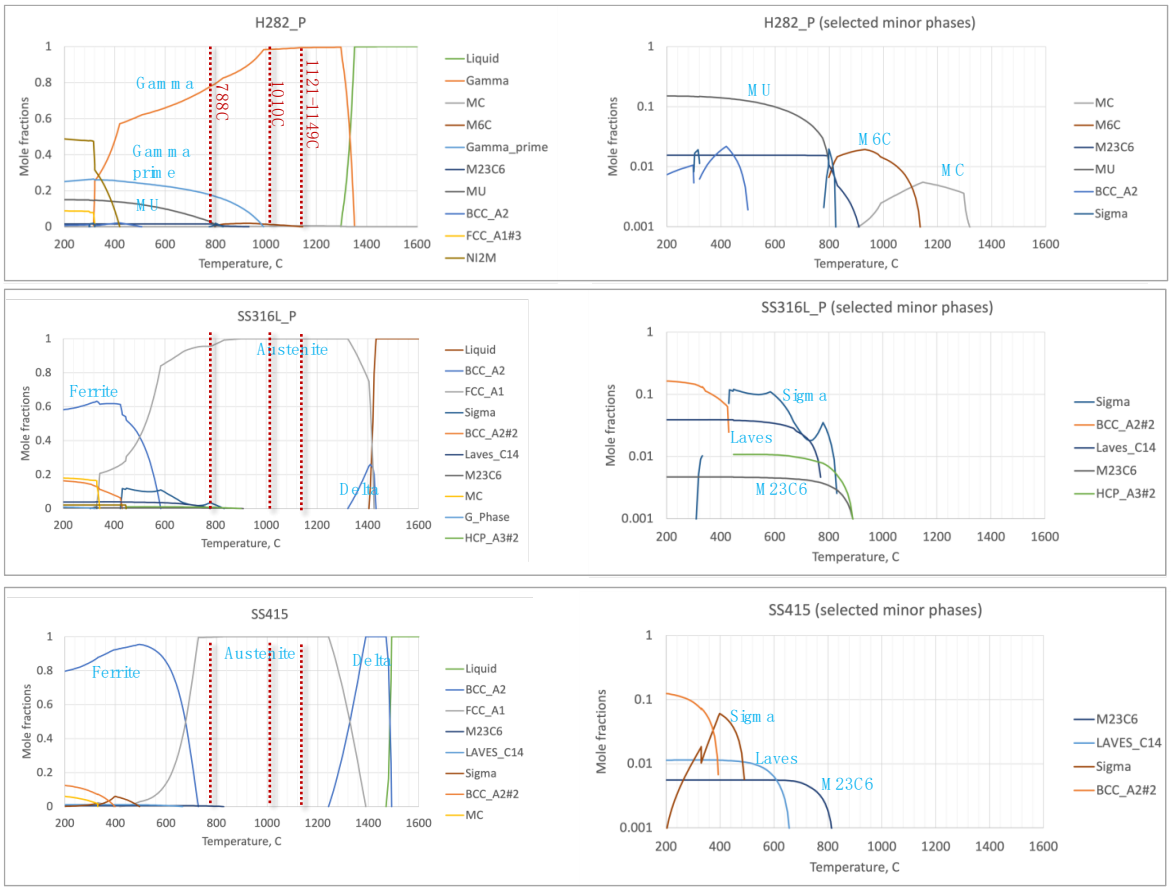

Figure 8. Calculated equilibrium phases.

3.4. Microstructure

Figure 9 displays representative microstructure in as-HIP state for 282/SS316L and SS316L/282 at the interface region. The applied powder vacuum heat treatment successfully created a slightly sintered "crust" of surface of the powder loaded in the bottom half of the HIP container. This crust effectively helped retain the flat shape of the powder surface during subsequent powder loading in the top half and vibrational packing. The well-defined interface observed in Figure 9 instead of mixed powder species is evidence of the sound process. The interface is relatively sharp and straight, as defined by the contours of individual powder. Consolidated 282 and SS316L on either side of the interface can be distinguished based on brighter and darker contrast in backscattered electron images. Close to the interface and on the 282 side, a dense distribution of dark-contrast discrete particles heavily decorate prior particle boundaries (PPBs) as well as inside powder particles. PPB particles in dark contrast also exist in the base metals, but in a much lower quantity and finer size. Comparing 282/SS316L and SS316L/282, powder loading sequence and vacuum heat treatment temperature that vary in the two configurations do not exhibit an obvious difference in the as-HIP microstructure. It can be seen in Figure 9 that very low density of dark contrast PPB particles are present in the base metal of 282 and SS316L, away from the ~100 μm interface region.

As-HIP interface microstructure of 282/SS415#1, SS415#1/282, and 282/SS415#2 is shown in Figure 10. A relatively sharp and straight interface was also visualized by the contrast difference of 282 and SS415. SS415 base shows a lath structured martensite within prior austenite grains. Compared to 282/SS316L alloy combination, a major difference in the interface microstructure of 282/SS415 alloy combination is a lower density of PPB particles. The location of these PPB particles is approximately 20 μm off the interface and within the 282 side. The first and second batch of SS415 powder differs significantly in carbon content, however, no noticeable difference was observed in the microstructure including interface PPB distribution, consistent with interdiffusion simulation results. It can be seen in Figure 10 that very low density of dark contrast PPB particles are present in the base metal of 282 and SS415, away from the ~100 μm interface region.

Figure 11 presents the interface microstructure of 282/SS415#1 in the fully heat-treated state. The secondary electron image (Figure 11a) is able to distinguish two types of fine particles in sub-micron size range that decorate PPB in a mixed mode: dark contrast particles in higher fraction and bright contrast particles in lower fraction. The EDS map (Figure 11b) further identifies the major chemistry of the two PPB particles: dark contrast being Ti rich carbonitrides and bright contrast being Al rich oxides. Similarly, these two PPB particles were also observed in 282/SS316L interface, despite a difference in quantity.

The microstructure after full heat treatment is similar to as-HIP state in terms of grain size, PPB particle size, distribution, and type at steel/282 interface. Applied heat treatment changes secondary phases in the 282 base metal by setting the right size for γ' precipitates and forming M23C6 carbides along grain boundaries, similar to secondary phase distribution in fully heat treated wrought HAYNES® 282®.

Composition profiles in as-HIP SS316L/282 and SS415/282 were measured with electron probe microanalysis (EPMA). Line profiles were made to traverse joining interfaces, with about 250 microns on either side (an example is shown in Figure 12). A beam diameter of three microns and step size of three microns were used. Each line profile produced about 167 quantitative spot measurements of eight elements: Fe, Ni, Co, Cr, Al, Ti, Mo, and Mn.

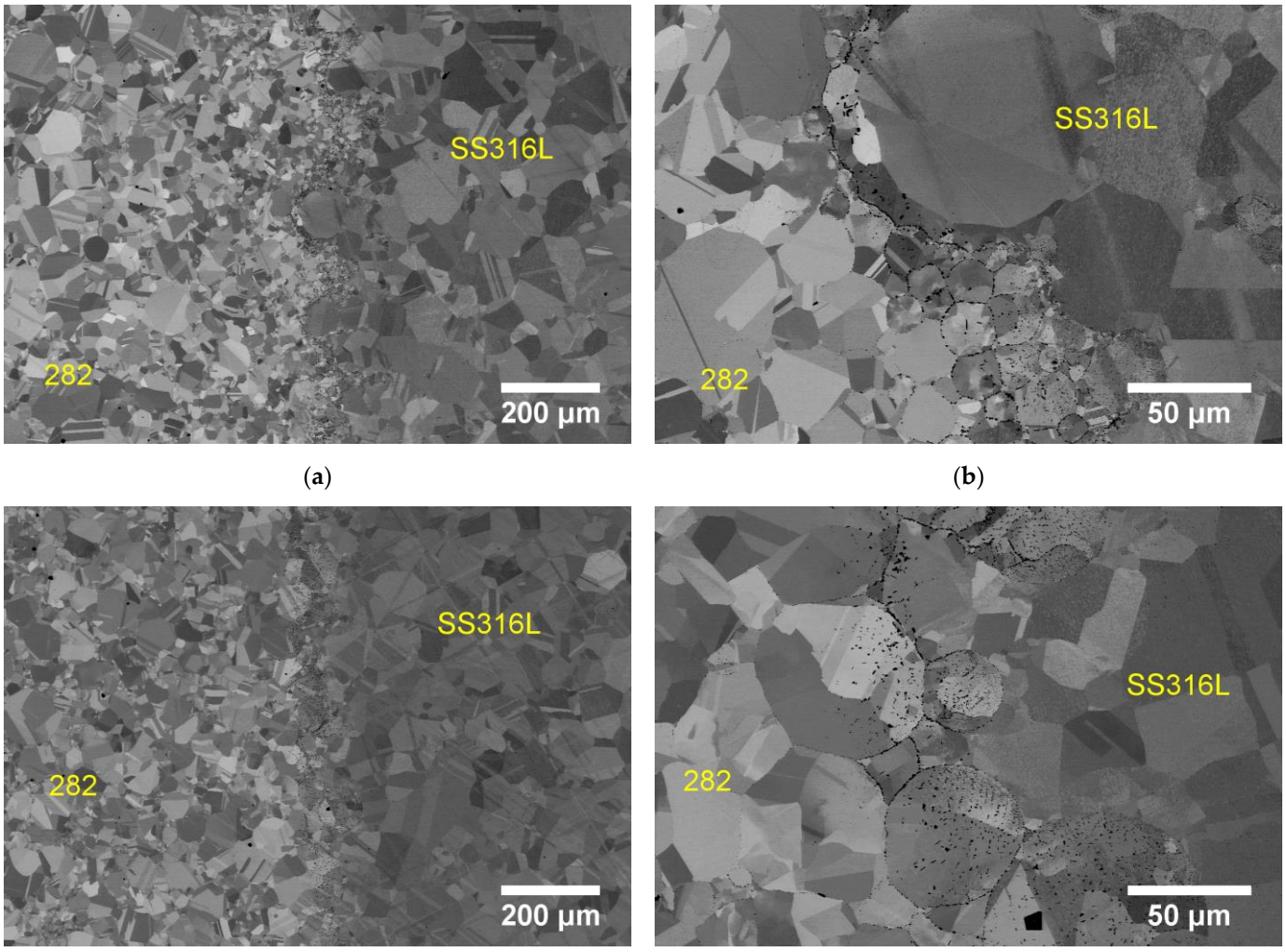

Figure 9. Backscatter electron images of representative microstructure in as-HIP 282/SS316L (**a**,**b**) and SS316L/282 (**c**,**d**).

Figure 13 shows two SS316L/282 samples with a different can-filling procedure, described in Table 2. The difference in the measured composition profiles is not significant because of the same HIP condition, except that 282/SS316L shows a small step at the SS316L side (50–100 microns from interface) simultaneously in all elements (most noticeably Co, Fe, Ni). Repeat measurements at two additional locations in 282/SS316L confirmed that the variation was caused by local protrusion of 282 powders into the SS316L side during powder packing (i.e., local interface is not flat).

Diffusion simulations were performed with the actual HIP temperature-time condition. The simulated profiles are included in Figure 13 for each element. There is a good agreement with the EPMA data. In the regions far away from interface (about 200 microns, in both directions) the compositions are close to the 'bulk' composition of the powders. Since the simulations used actual powder compositions, the agreement with EPMA data in the bulk regions is not unexpected. Nevertheless, minor differences are still observed in Mn on the SS316L side and in Co and Al on the 282 side, while a greater difference in Cr is seen overall (and among the EPMA data sets). These differences are attributed to EPMA standard calibration and should not alter the conclusions here. A closer look at the Al profiles also indicates a small over-shoot near the interface (at the 282 side) in both simulation and EPMA.

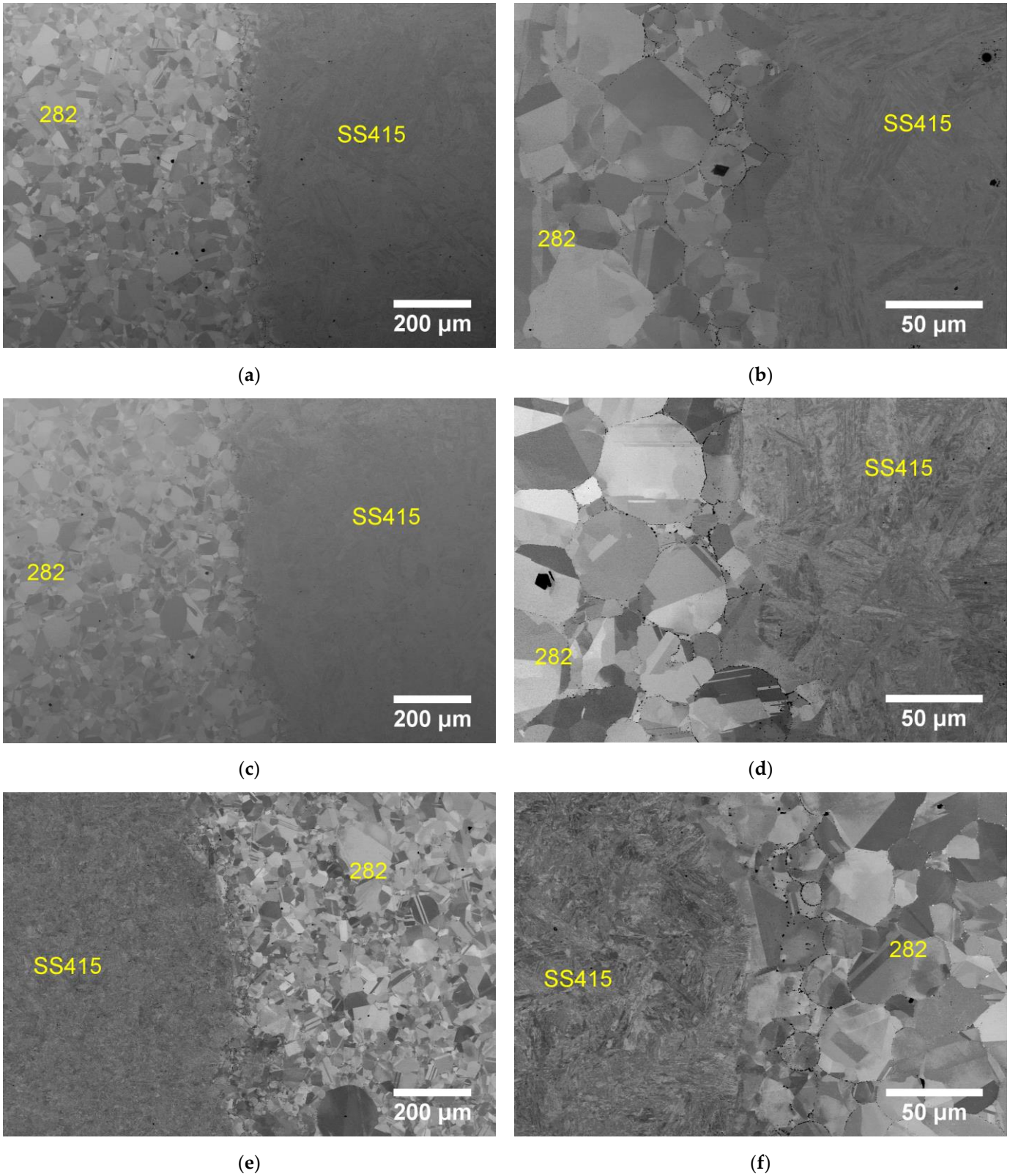

Figure 10. Backscatter electron images of representative microstructure in as-HIP 282/SS415#1 (**a**,**b**), SS415#1/282 (**c**,**d**), 282/SS415#2 (**e**,**f**).

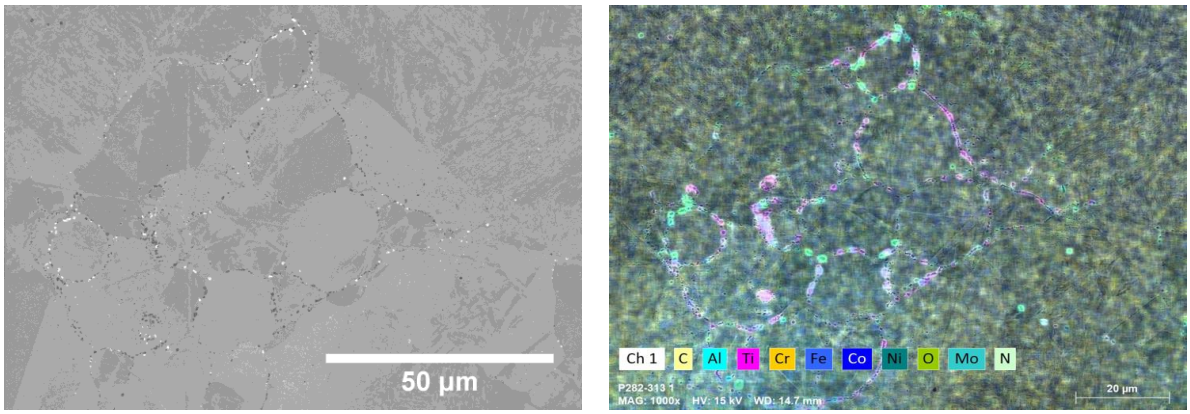

(**a**) (**b**)

Figure 11. Secondary electron image (**a**) and EDS map (**b**) of 282/SS415#1 interface region after full heat treatment.

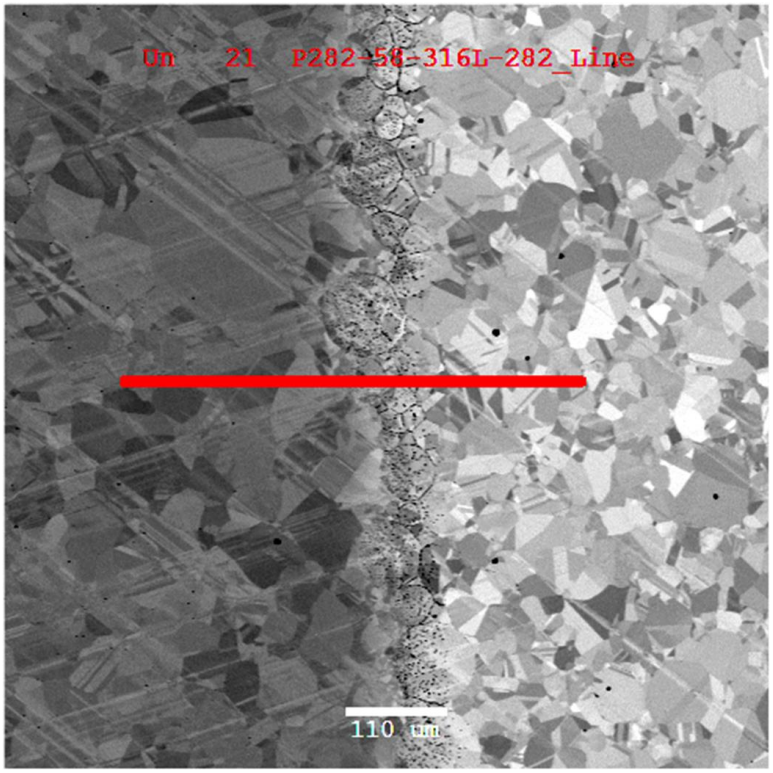

Figure 12. Location of EPMA measurement on the sample SS316L/282 (red line). SS316L is on the left, 282 is on the right.

Although the interstitial elements C and N were not measured in EPMA and were unavailable for comparison with simulation, the EPMA's Ti data give some indirect evidence, as Ti is a forming element of M (C,N) carbide (carbonitride) phase. Near interface, the Ti data show a significant scatter because the EPMA's small incident beam (three micron) hits matrix phase or MC carbides, which have large difference in Ti compositions. The scatter is obvious because the local MC amount is high. The band of data scatter is approximately the width of the excess MC particles (thus C and N) formed at the interface. Figure 14 overlays these data with the simulated MC carbide fraction. The width of the interested region (~50 microns at interface) agrees very well between the EPMA and simulation. It is also noted that this is the latest evidence that the formation of these PPB particles is mainly on the 282 side.

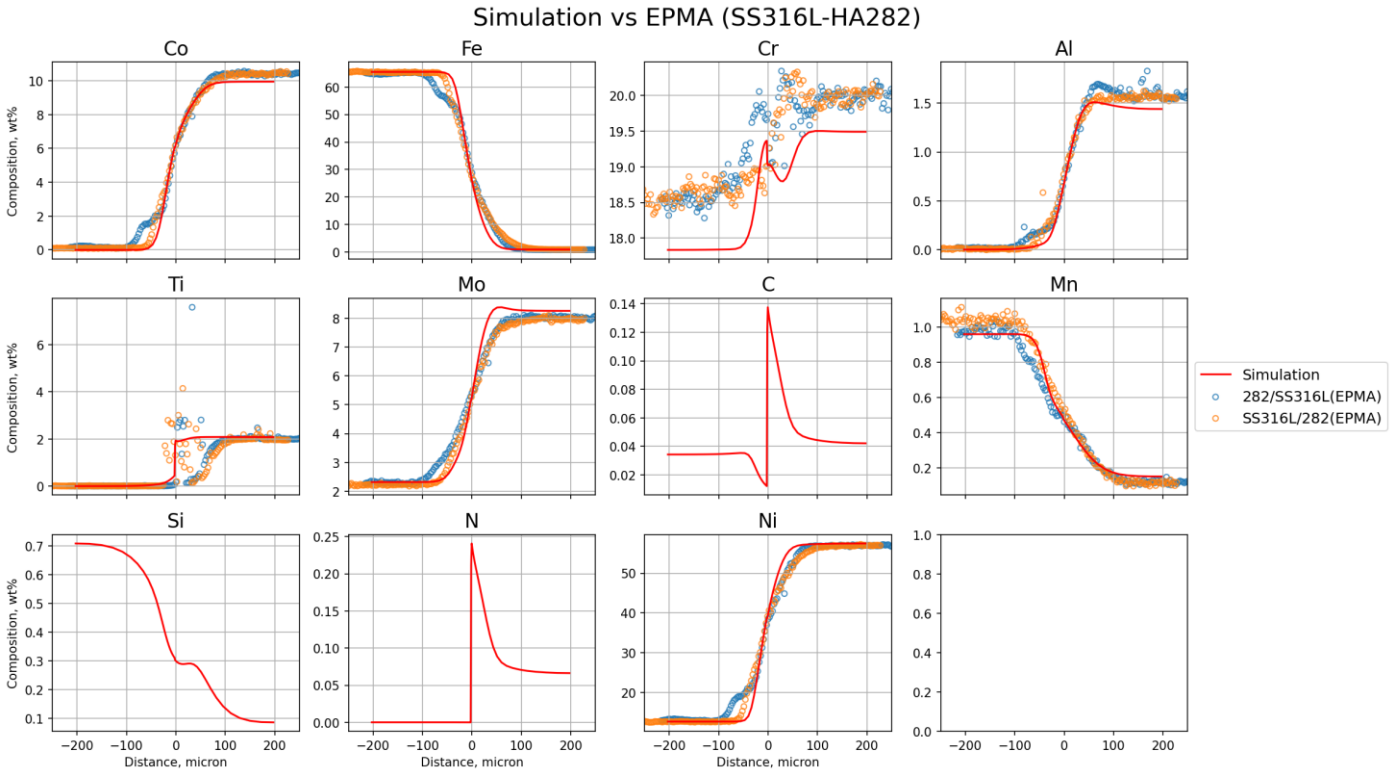

Figure 13. EPMA measurements and the simulated composition profiles between SS316L (**left**) and 282 (**right**) at 1204 °C (HIP temperature). Joining interface is at distance zero.

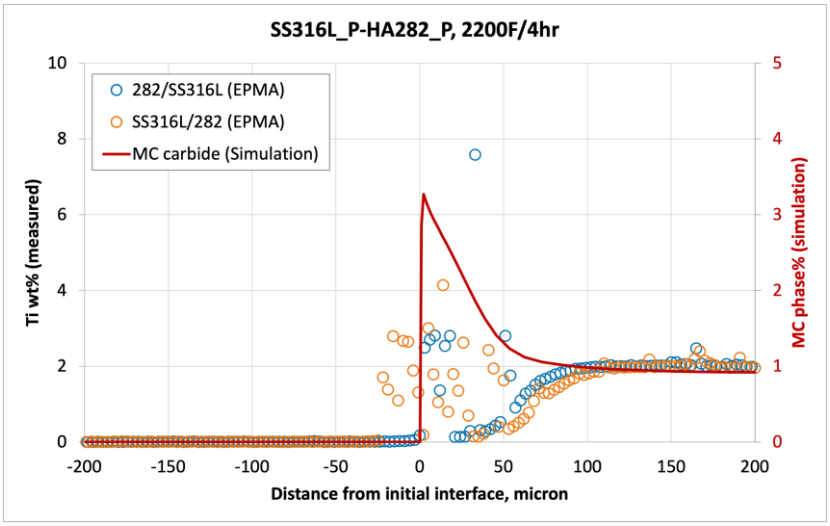

Figure 14. Overlay of scattered EPMA Ti data and simulated MC carbide profile. Data scatter is an indication of excess MC carbides near interface, agrees well with the simulation.

Figure 15 shows an overlay of the EPMA measurement and simulated composition profiles in SS415#1/282 samples. Similar to SS316L/282, the three SS415#1/282 samples using different can-filling procedures have only small difference in the measured composition profiles. A good agreement between EPMA data and simulation is also seen in SS415#1/282 samples. The amount of excess MC particles inferred from the scatter in EPMA Ti signal is much less in SS415#1/282 as compared to the SS316L/282 samples. This is consistent with the observation of less PPBs at SS415#1/282 joint interface from the SEM images reported previously.

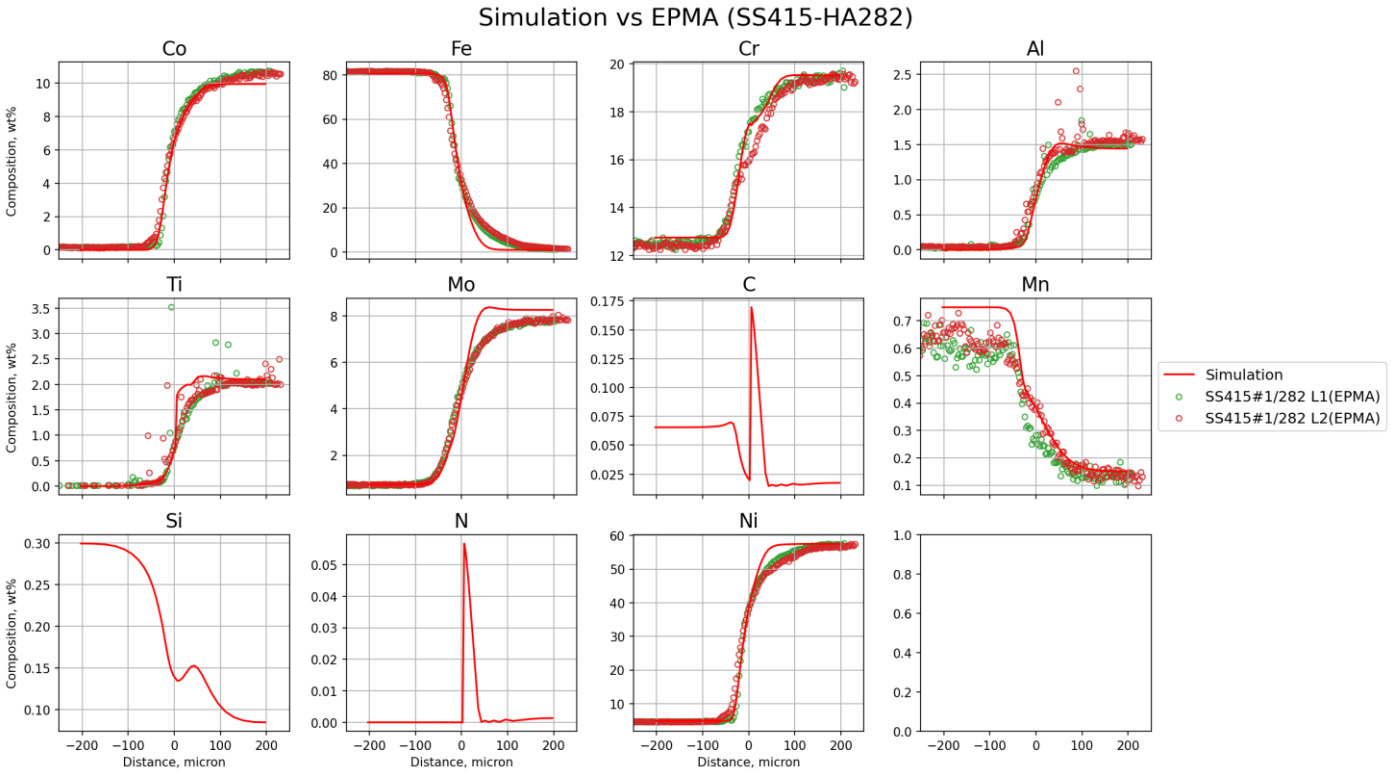

Figure 15. EPMA measurements (SS415#1/282, two line-profiles) and simulated composition profiles between SS415 (**left**) and Alloy 282 (**right**) at 1204 °C (HIP temperature). Joining interface is at distance zero.

3.5. Tensile Property

Figure 16 summarizes tensile properties of PM HIP 282 base metal, SS316L base metal, and two bimetallic cross interface configurations in comparison to wrought HAYNES® 282® and cast CF8M (cast SS316) [30]. Each data point represents one tensile test. Most 282/SS316L and SS316L/282 bimetallic specimens fail near or at the interface location (Figure 17a), except for two specimens tested at 400 °C. 282/SS316L and SS316L/282 bimetallic specimens show comparable yield strength as PM HIP SS316L base metal and cast CF8M. They have slightly lower ultimate tensile strength (UTS) than SS316L base metal, while still being comparable to cast CF8M. Consistent with our previous work [2], PM HIP 282 base metal shows slightly higher yield strength and UTS than wrought HAYNES® 282®, and its strength is much higher than SS316L base and bimetallic specimens. Powder loading sequence and vacuum heat treatment condition in the bimetallic HIP capsules do not generate any major differences in yield strength and UTS. Note that UTS of 282/SS316L and SS316L/282 bimetallic specimens are all significantly lower than yield strength of 282 base metal, indicating that the 282 half in the bimetallic specimens probably experienced little to no plastic deformation under the maximum tensile loading. Typical fracture surface of most bimetallic specimens that failed at interface reveals powder particle contours and fracture along PPBs (Figure 17b as one example). This implies that the dense distribution of Ti-rich carbonitrides along PPBs (Figure 9) as a result of interdiffusion during HIP cycle weakens the HIP bonding of dissimilar alloys and causes tensile failure.

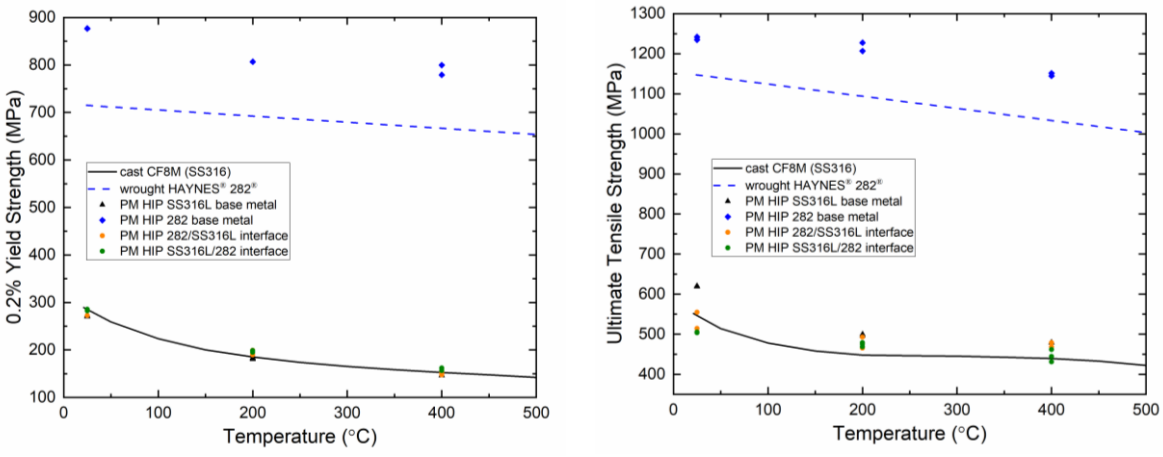

(**a**) (**b**)

Figure 16. 0.2% tensile yield strength (**a**) and ultimate tensile strength (**b**) of PM HIP SS316L, 282, and 282/SS316L interface in comparison with wrought HAYNES® 282® and cast CF8M (SS316).

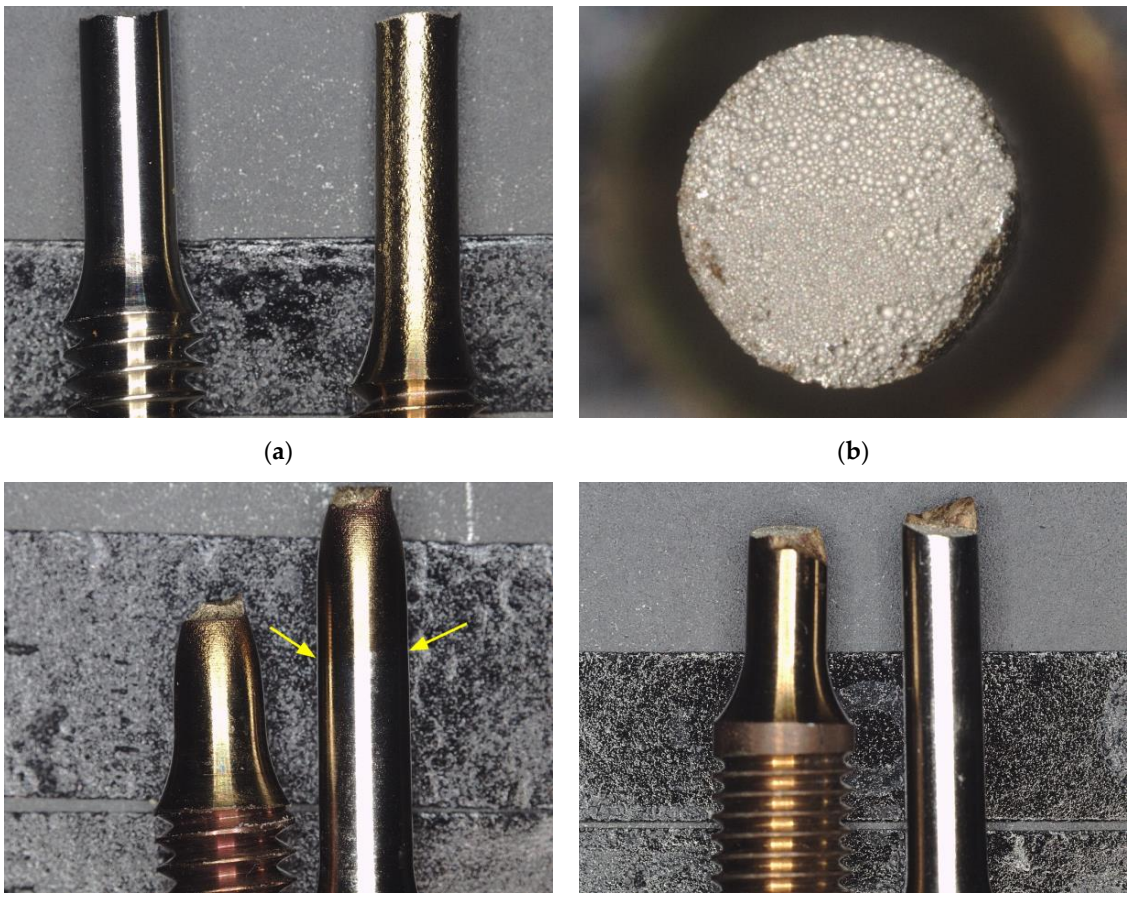

(**a**) (**b**)

(**c**) (**d**)

Figure 17. Keyence optical images of tensile ruptured specimens and fracture surface: (**a**,**b**) SS316L/282 400 °C tested; (**c**) 282/SS415#1 400 °C tested (yellow arrows indicating the interface between two alloys); (**d**) SS415#2/282 400 °C tested.

Tensile results of 282/SS415 configurations are plotted in Figure 18. The first and second lot of SS415 powder with low and high carbon content result in quite different mechanical properties. Using the first powder lot, all the 282/SS415#1 and SS415#1/282 bimetallic

specimens failed within the SS415 base metal, indicating that the interface strength was higher than SS415#1 base metal. Figure 17c shows one example of a 400 °C tensile ruptured specimen, where discoloration of SS415 due to oxidation and lack of discoloration in 282 clearly visualizes the interface location as pointed by yellow arrows. Additional metallography analysis on the longitudinal cross sections observed no microcrack or microvoid damage at the interface, confirming a good bonding. Yield strength and UTS of bimetallic specimens are slightly higher than SS415#1 base. It is believed that having a lower fraction of carbonitrides at 282/SS415 interface (Figure 10) than 282/SS316L interface (Figure 9) contributes to a higher metallurgical bonding that prevents interface rupture. Absent of interface failure, the difference in the powder heat treatments cannot be identified. The 600 °C/1 h tempering treatment added after the second aging step was intended to increase toughness, while strength of SS415#1 unfortunately dropped below that of cast CA6NM (cast SS415) [30] possibly without sufficient carbon content in the first powder lot.

The second SS415 powder lot results in substantially higher yield strength and UTS in SS415#2 base metal than the first powder lot, possibly due to higher carbon content. Using a standard 282 heat treatment without tempering, tensile strength of SS415#2 and SS415#2/282 both outperform that of cast CA6NM. However, the bimetallic specimens present a property penalty in yield strength and UTS compared to SS415#2 base metal, leading to tensile failures around interface. Interestingly, several test specimens had fractured surfaces in partial 282 and partial SS415#2 base metals (one example shown in Figure 17d). Not all the test specimens failed along the interface. The lower density of PPB precipitates near interface (Figure 10) probably reduces the chance of tensile rupture along these PPB networks.

Given the strength requirement of the target component, 282/SS415#2 alloy combination with typical HAYNES® 282® heat treatments are downselected for the dual alloy pipe demonstration. SS316L base metal and 282/SS316L interface do not have sufficient strength.

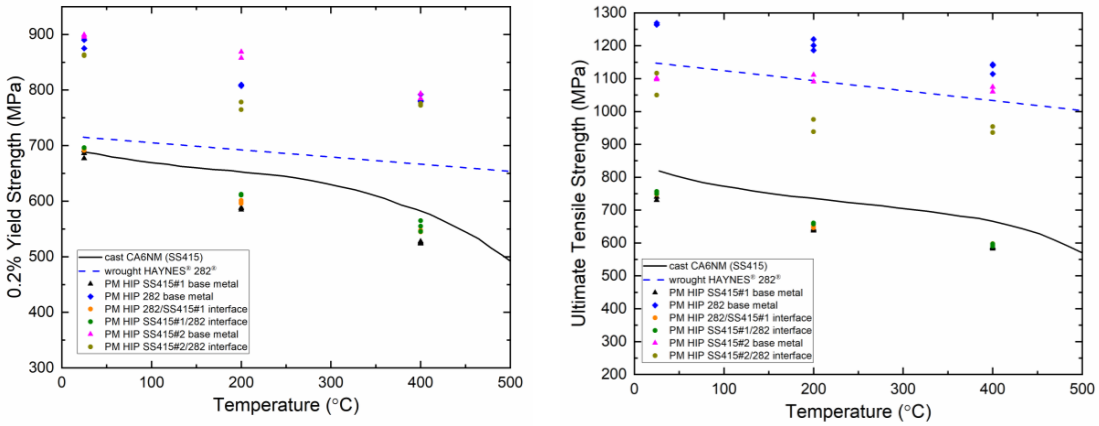

(**a**) (**b**)

Figure 18. 0.2% tensile yield strength (**a**) and ultimate tensile strength (**b**) of PM HIP SS415, 282, and 282/SS415 interface in comparison with wrought HAYNES® 282® and cast CA6NM (SS415).

3.6. Bimetallic PM HIP Pipe Demonstration

Leveraging lessons learned from the lab-scale study, a bimetallic SS415#2/282 pipe in 10.75 inch outer diameter, 1 inch wall thickness, 8.75 inch inner diameter, and 8 inch length was demonstrated to show the scale-up feasibility. The four technological challenges were to be met during this demonstration:

- Providing the dimensionally controlled location of the two alloys in the pipe;
- Formation of the firm and well-controlled interface between the two alloys;
- HIP both alloys to 100% density;
- Achieving the overall dimensions of the bimetal pipe.

To achieve these goals, the HIP capsule was designed by accounting for the different rheology of the two powders: 282 and SS415#2. A proprietary HIP model that considered non-uniform shrinkage during powder HIP was applied to back calculate the required HIP capsule dimension. In this case, a straight hollowed pipe was used as the HIP capsule for low cost and easy fabrication. To form a firm and well-controlled interface, the bottom half of the HIP capsule was first filled with 282 powder and then vacuum pre-sintered at 1204 °C to form a "crust" on the surface. Right before being loaded in the vacuum furnace, the HIP capsule was subjected to additional vibration to level the powder and the top was kept open for convenient inspection. After powder heat treatment, SS415#2 powder was loaded on top of 282 powder and the same HIP cycle (1204 °C/15 ksi/4 h) was applied. Figure 19a,b show the successfully HIPed capsule with a flat interface as a transition of OD and ID of the pipe. Figure 19c displays the measured dimension which nicely envelopes the target pipe dimension and allows for post machining. Powder packing density and material strength at HIP temperature determined more shrinkage in SS415#2 powder than 282 powder. The HIPed capsule was then machined into the final dimension of bimetallic pipe, which showed good machinability across the interface. Then, 282 heat treatment of solution and two-step aging was applied. Afterwards, the pipe was inspected by dye penetrant showing no cracks and defects particularly at SS415#2/282 interface (Figure 19d). SS415#2 material in the fill stems were examined by optical microscopy to confirm full consolidation through HIP and no thermally induced porosity (TIP). These results validate a successful demonstration of bimetallic HIP pipe that meets all the technical challenges.

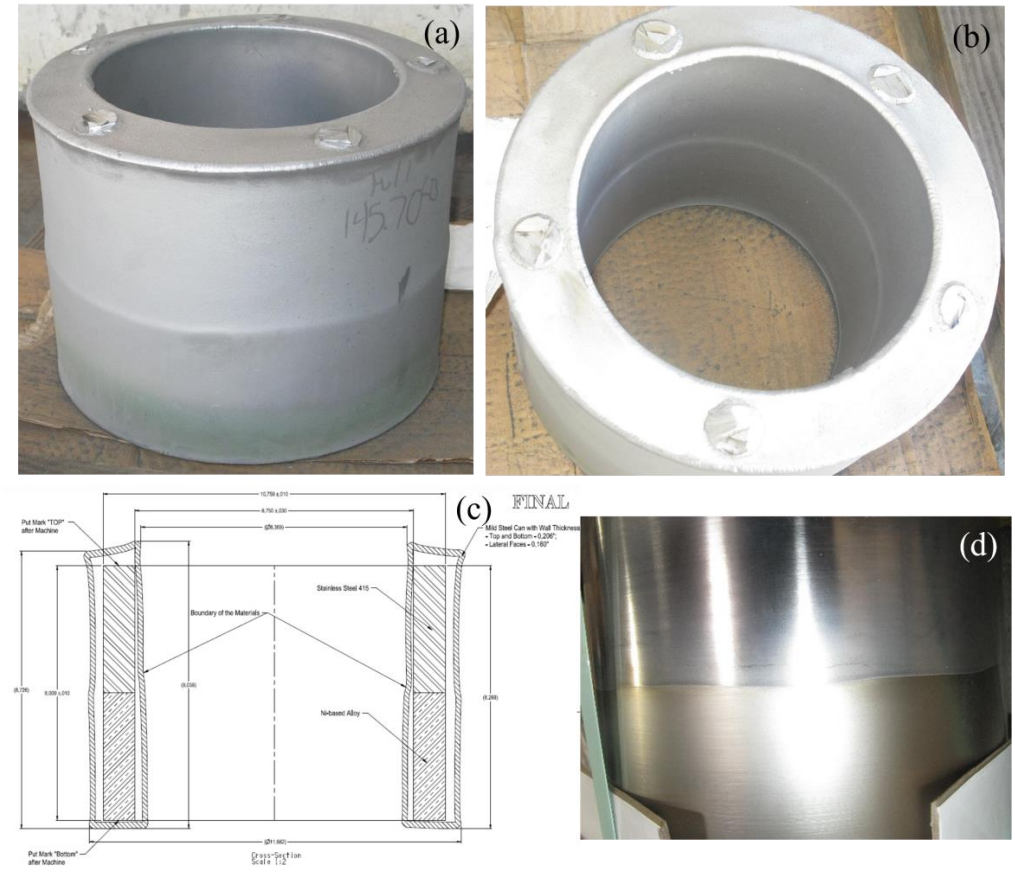

Figure 19. (**a**) Bimetallic pipe with HIP capsule material in as-HIP state: top half is consolidated SS415 powder, bottom half is consolidated 282 powder, interface is straight; (**b**) top-down view of inner diameter where interface is clearly seen; (**c**) measured post-HIP dimension (with capsule material) overlayed on top of target dimension of the bimetallic pipe; (**d**) closer view of interface after machining to the final dimension and applying heat treatment.

4. Conclusions

Feasibility in the HIP manufacturing of an integral bimetallic component using dissimilar alloy powder was investigated for 282/SS316L and 282/SS415 combinations. Interdiffusion profile at dissimilar alloy interface caused by the HIP cycle is predicted by DICTRA simulations and validated by EPMA analyses. Interdiffusion distance of most elements is around 100 μm, while C and N have a higher interdiffusion distance. Dense distribution of Ti-rich carbonitrides and alumina particles are found to decorate prior particle boundaries near the interface on the 282 side, affecting tensile strength across interface as well as tensile failure location. A higher amount of excessive carbonitride formation near interface is observed in SS316L/282 than SS415/282, consistent with the predicted greater influence of interdiffusion in SS316L/282. Typical HAYNES® 282® heat treatment condition is applicable to 282/SS316L and 282/SS415 combinations, resulting in higher strength than CF8M (cast SS316) and CA6NM (cast SS415). A pilot-scale bimetallic SS415/282 pipe has been then developed and demonstrated to show the promise of scale-up. The technological requirements of dimensional control of the two alloys and interface, defect-free interface by dye penetrant inspection, good machinability across interface, and microstructure are all met.

Author Contributions: Conceptualization, S.H.; methodology, S.H., V.S. and C.S.; validation, C.S. and V.S.; investigation, S.H., V.S. and C.S.; data curation, S.H.; writing—original draft preparation, S.H. and C.S.; writing—review and editing, V.S.; funding acquisition, S.H. All authors have read and agreed to the published version of the manuscript.

Funding: This work was funded by US Department of Energy, Energy Efficiency and Renewable Energy, Solar Energy Technology Office under award DE-EE0008996. GE Research provided cost share.

Data Availability Statement: The raw data supporting the conclusions of this article will be made available by the authors on request.

Acknowledgments: The authors thank Haynes International for HAYNES® 282® wire and AP&C (GE Additive) for plasma atomizing 282 powder. The authors would like to acknowledge technical support from Daniel Ruscitto, Marija Drobnjak, Robert Campbell, Chris Perlee, Chris Mclasky at GE Research.

Conflicts of Interest: Authors Shenyan Huang and Chen Shen were employed by the company GE Research. Author Victor Samarov was employed by the company Synertech PM (United States). All authors declare that the research was conducted in the absence of any commercial or financial relationships that could be construed as a potential conflict of interest.

References

1. Marion, J.; Macadam, S.; McClung, A.; Mortzheim, J. The STEP 10 MWe sCO2 Pilot Demonstration Status Update. In Proceedings of the ASME Turbo Expo 2022: Turbomachinery Technical Conference and Exposition, Rotterdam, The Netherlands, 13–17 June 2022; Volume 9: Supercritical CO_2; V009T28A034; ASME: New York, NY, USA, 2022. [CrossRef]
2. Huang, S.; Samarov, V.; Seliverstov, D.; Mortzheim, J.; Khomyakov, E. Near-Net-Shape HIP Manufacturing for sCO2 Turbomachinery Cost Reduction. In Proceeding of the 13th International Conference on Hot Isostatic Pressing: HIP'22, Columbus, OH, USA, 11–14 September 2022; Materials Research Proceedings 2023. Volume 38, pp. 11–16. [CrossRef]
3. Walker, R.M.; Roberts, D.J.; Rickinson, B.A. Component assembly using HIP diffusion bonding. In *Diffusion Bonding 2*; Stephenson, D.J., Ed.; Springer: Dordrecht, The Netherlands, 1991; pp. 261–269. [CrossRef]
4. Fu, H.Y.; Nagasaka, T.; Muroga, T.; Kimura, A.; Chen, J.M. Microstructural characterization of a diffusion-bonded joint for 9Cr-ODS and JLF-1 reduced activation ferritic/martensitic steels. *Fusion Eng. Des.* **2014**, *89*, 1658–1663. [CrossRef]
5. Hammelmann, K.H.; Buchkremer, H.P.; Stöver, D. HIP-diffusion bonding of ODS-materials by use of plasma sprayed encapsulation. In *Diffusion Bonding 2*; Stephenson, D.J., Ed.; Springer: Dordrecht, The Netherlands, 1991; pp. 250–260. [CrossRef]
6. Nagasaka, T.; Fu, H.; Muroga, T.; Tanaka, T.; Sagara, A.; Guan, W.; Nogami, S.; Hasegawa, A.; Serizawa, H.; Kimura, A.; et al. *Development of Dissimilar-Metals Joint of Oxide-Dispersion-Strengthened (ODS) and Non-ODS Reduced-Activation Ferritic Steels (IAEA-N-234)*; International Atomic Energy Agency (IAEA): Vienna, Austria, 2018.
7. Auger, J.P.; Raisson, G.; Pierronnet, M. Design and manufacture of engineered components clad by HIP. In *Hot Isostatic Pressing—Theory and Applications: Proceedings of the Third International Conference*; Koizumi, M., Ed.; Springer: Dordrecht, The Netherlands, 1992; pp. 229–234. [CrossRef]

8. Theisen, W. Hip cladding of tools. In *Proceeding of the 6th International Tooling Conference*; Bergström, J., Ed.; Karlstad University: Karlstad, Sweden, 2002; pp. 947–960.
9. Gauthier, M.; D'Amours, G.; Bernier, F. HIP Processing of Improved Tooling Materials for High-Productivity Hot Metal Forming Processes. In Proceeding of the 12th International Conference on Hot Isostatic Pressing: HIP'17, Sydney, Australia, 5–8 December 2017; Materials Research Proceedings 2019; Volume 10, pp. 85–91. [CrossRef]
10. Masahashi, N.; Hanada, S. Effect of pressure application by HIP on microstructure evolution during diffusion bonding. *Mater. Trans.* **2005**, *46*, 1651–1655. [CrossRef]
11. Butrim, V.N.; Beresnev, A.G.; Denisov, V.N.; Klyatskin, A.S.; Medvedev, D.A.; Makhina, D.N. Experience in HIP diffusion welding of dissimilar metals and alloys. In Proceedings of the 12th International Conference on Hot Isostatic Pressing: HIP'17, Sydney, Australia, 5–8 December 2017; Materials Research Proceedings 2019; Volume 10, pp. 65–72. [CrossRef]
12. Magerramova, L.A. Achievement of bimetallic blisks integrated dissimilar alloys for promising high temperature aviation gas turbine engines. In Proceedings of the 28th Congress of the International Council of the Aeronautical Sciences 2012, Brisbane, Australia, 23–28 September 2012; Volume 3, pp. 2457–2465.
13. Magerramova, L.; Kratt, E. Development of the Design and Technological Solutions for Manufacturing of Turbine Blisks by HIP Bonding of the PM Disks with the Shrouded Blades. In Proceedings of the 12th International Conference on Hot Isostatic Pressing: HIP'17, Sydney, Australia, 5–8 December 2017; Materials Research Proceedings 2019; Volume 10, pp. 39–46. [CrossRef]
14. Locci, I.E.; Nesbitt, J.A.; Ritzert, F.J.; Bowman, C.L. High temperature stability of dissimilar metal joints in fission surface power systems. *AIP Conf. Proc.* **2007**, *880*, 660–667. [CrossRef]
15. Zhang, L.W.; Fu, H.Y.; Chai, Z.J.; Zheng, P.F.; Wei, R.; Zhang, M.; Chen, J.M. Dissimilar-metal bonding of a carbide-dispersion strengthened vanadium alloy for V/Li fusion blanket application. *Tungsten* **2020**, *2*, 101–106. [CrossRef]
16. Xiao, Y.; Lang, L.; Xu, W.; Zhang, D. Diffusion bonding of copper alloy and nickel-based superalloy via hot isostatic pressing. *J. Mater. Res. Technol.* **2022**, *19*, 1789–1797. [CrossRef]
17. Dineshraj, S.; Manwatkar, S.K.; Gupta, R.K.; Bajargan, G. Development of hot isostatic pressing technology for joining multiple joints of dissimilar materials of stainless steels with IN 718 and Ti-6Al-4V. *Trans. Indian Inst. Met.* **2024**. [CrossRef]
18. Stavroulakis, E.; Bowden, D.; Irukuvarghula, S.; Garner, A.; Pickering, E.; Stewart, D.; Preuss, M. Characterisation of ferritic to austenitic steel functional grading via powder hot isostatic pressing. *Mater. Today Commun.* **2022**, *31*, 103442. [CrossRef]
19. Stavroulakis, E.; Irukuvarghula, S.; Pickering, E.; Stewart, D.; Preuss, M. Fundamental aspects of functional grading via powder hot isostatic pressing–Development of microstructure and diffusional processes. *Mater. Des.* **2022**, *215*, 110437. [CrossRef]
20. Zhu, W.; Liu, W.; Ma, Y.; Cai, Q.; Wang, J.; Duan, Y. Microstructural characteristics, mechanical properties and interfacial formation mechanism of tungsten alloy/steel composite structure fabricated by HIP co-sintering. *Mater. Des.* **2021**, *211*, 110127. [CrossRef]
21. Lister, S.; Blanch, O.L.; Fernandez, D.S.; Pope, J.; Baxter, G.J.; Bray, S.; Jackson, M. A Machinability Assessment of the Novel Application of Field-Assisted Sintering Technology to Diffusion Bond (FAST-DB) and Functionally Grade Dissimilar Nickel-Based Superalloys. *Metall. Mater. Trans. A* **2023**, *19*, 1–3. [CrossRef]
22. Larker, R.; Ockborn, J.; Selling, B. Diffusion bonding of CMSX-4 to UDIMET 720 using PVD-coated interfaces and HIP. *J. Eng. Gas Turbines Power.* **1999**, *121*, 489–493. [CrossRef]
23. Buchkremer, H.P.; Ennis, P.J.; Stover, D. Manufacture and stress rupture properties of hipped austenitic-ferritic transition joints. *J. Mater. Process. Technol.* **1999**, *92–93*, 368–370. [CrossRef]
24. Guelman, A.A. HIP diffusion bonding of intricate shape components made of light alloys and steels. In *Proceedings of the KWS Conference*; The Korean Welding and Joining Society: Daejeon, Republic of Korea, 2002; pp. 769–775.
25. Bassini, E.; Vola, V.; Lorusso, M.; Ghisleni, R.; Lombardi, M.; Biamino, S.; Ugues, D.; Vallillo, G.; Picqué, B. Net shape HIPping of Ni-superalloy: Study of the interface between the capsule and the alloy. *Mater. Sci. Eng. A* **2017**, *695*, 55–65. [CrossRef]
26. Frisk, K.; Luo, C.; Johansson, S.C.; Haglund, S.; Petterson, N.; Strandell, I. Compound materials by PM-HIP. *Powder Metall.* **2014**, *57*, 341–347. [CrossRef]
27. Le, J.; Yang, J.; Yin, H.; Samarov, V.; Gandy, D.; Lou, X. SA508 low alloy steel to 316L stainless steel dissimilar metal joint made by powder metallurgy hot isostatic pressing. *Mater. Sci. Eng. A* **2023**, *875*, 145060. [CrossRef]
28. Burlet, H.; Martinez, M.; Cailletaud, G. Microstructure and residual stresses issued from the bonding of an austenitic onto a ferritic steel by solid diffusion. In Proceedings of the 4th European Mechanics of Materials Conference on Processes, Microstructures and Mechanical Properties, Metz, France, 11 September 2001; Volume 11, pp. 157–164. [CrossRef]
29. Weiss, B.F.; Strickler, R. Phase Instabilities during High Temperature Exposure of 316 Austenitic Stainless Steel. *Metall. Trans.* **1972**, *3*, 851–866. [CrossRef]
30. Blair, M.; Stevens, T.L. *Steel Casting Handbook*, 6th ed.; Steel Founders' Society of America: Crystal Lake, IL, USA, 1995.